ADVANCED FUNCTIONAL MATERIALS
www.afm-journal.de

Anti-Swelling Textile Power Generator with 1D Nanoscale Channel Alignment in Nanofiber/Graphene Hybrid Yarns

Yuman Zhou, Xiaohan Shi, Meng An, Kai Weng, Zhihao Lei, Qing Zhang, and John Haozhong Xin**

Perspiration transpiration-induced electrical generator offers an innovative solution for developing self-powered intelligent textiles, enabling the seamless integration of emerging technologies into daily routine, however their performance is often constrained by inefficient water transport in tortuous channels and structural instability caused by water swelling. Inspired by vascular bundle in *Neottopteris antiqua*, a nanoassembly strategy is proposed to fabricate nanofiber/nanosheet hybrid yarn through bath electrospinning. The yarn exhibited an excellent 1D oriented nanoscale channel structure and exceptional weaving ability. Subsequent functionalization strategies imparting cross-linking feature to the nanofiber/graphene yarn yielded consistent structure and remarkable water anti-swelling capability, maintaining structural stability even after 10 days of water immersion. Further assembled into a TEG, a single 4-cm-long yarn demonstrated the output voltage of 295 mV and current of 1.82 µA in a water environment, which increased to 360.4 mV and 2.57 µA under simulated perspiration conditions. When configured into a waterproof fabric through series-parallel connection of 62-cm yarns, an enhanced output voltage of 1.85 V is achieved, sufficiently powering small electronic devices such as lamp bead and display screen. This study highlights the yarns' remarkable potential for robust and efficient applications in next-generation self-powered intelligent textiles.

1. Introduction

Self-powered intelligent products are crucial for overcoming environment and energy limitations. Recent years, wearable transpiration-induced electrical generators (TEGs) have attracted significant attention for their ability to sustainably generate electricity through selective ion transport driven by capillary action and water potential gradients, prominently eliminating the need for external energy input.[1,2] Fabrics, constructed from regularly stacked fibers with uniformly connected channels, inherently exhibit advantages for building TEGs due to their structural characteristics.[3,4] However, fabric-based TEGs depend on maintaining a humidity gradient between their two ends, which complicates their practicality in wearable applications. Additionally, integrating functional components into fabrics via immersion, brushing, printing, or dipping often leads to detachment issues. In comparison, yarns present a viable mode for wearable TEGs, as their ends can be easily controlled in textiles, and functional components can be directly embedded into yarns during spinning to ensure firmness. Notably, most current research on yarn-based TEGs focuses on wet-spun (WS) yarns, carbon nanotube (CNT) yarns, or graphene oxide (GO) yarns.[5–7] However, WS yarns, composed of continuous filaments ranging from several micrometers to hundreds of micrometers in diameter, lack the intrinsic channel structures found in short-fiber yarns. Even with solvent evaporation

Y. Zhou, J. H. Xin
School of Fashion and Textiles
The Hong Kong Polytechnic University
Hong Kong, China
E-mail: john.xin@polyu.ed.hk
Y. Zhou, X. Shi, Q. Zhang
Research Institute of Textile and Clothing Industries
Zhongyuan University of Technology
Zhengzhou, China
M. An
Department of Mechanical Engineering
The University of Tokyo
Tokyo, Japan
E-mail: anmeng@photon.t.u-tokyo.ac.jp
K. Weng
Graduate School of Medicine
Science and Technology
Shinshu University
Ueda, Japan
Z. Lei
Global Innovative Centre for Advanced Nanomaterials
The University of Newcastle
New South Wales, Australia

The ORCID identification number(s) for the author(s) of this article can be found under https://doi.org/10.1002/adfm.202510758

DOI: 10.1002/adfm.202510758

creating microporous networks, achieving consistent control over channel continuity, uniformity, and linearity remains challenging. Comparatively, self-assembled channels in low-dimensional CNT and GO yarns demonstrate superior potential and advantage for channel formation compared to artificial channel in WS yarns, which empowers prominent electrical output capability.

Transpiration, a naturally physical process in plants, enables continuous water absorption and transport via vascular bundles composed of hydrophilic wood fibers and 1D oriented channels, as found in species like *Neottopteris antiqua*.[8] Capillary forces drive water upward through these 1D channels, ensuring continuous water transport.[9] Inspired by the transpiration mechanism and grounded in the electric double layer (EDL) theory, various substrates and channels have been explored to enhance water absorption and transport, thereby improving electricity generation efficiency.[10,11] Recent advancements have been widely recognized that 1D oriented nanoscale channels formed in low-dimensional nanomaterials significantly improve energy output, as their high specific area and narrow interconnected linear channels can enhance water diffusion, evaporation, and EDL formation, thereby boosting energy conversion efficiency.[12–14] For example, Lee et al. showed the channels in GO films accelerate evaporation and energy harvesting by alleviating capillary evaporation limit.[15] Liang et al. reported ion transport along GO yarn channel outperforms layer-based transport.[7] Similarly, CNT yarn-based TEGs achieved superior electrical performance over film-based designs due to their ordered channels.[16] Zhao et al. also emphasized vertically aligned pores for optimizing moisture-driven energy generation.[17] Nevertheless, the imperative drawback lies in the self-assembly process of low-dimensional nanomaterials into yarns, which faces scalability limitations due to manufacturing challenges.

Nanofibers offer distinct advantages for TEGs, including high specific surface area, large aspect ratio, exposed functional group, and accessible interlayer channels, all of which can promote rapid water transport and efficient energy conversion.[18–20] Notably, the achieving of nanofibers via electrospinning is simplicity, cost-effectiveness, and scalability, which avoid the manufacturing challenges faced by CNT or GO yarns.[21] Meanwhile, 1D oriented nanoscale channels in electrospinning nanofiber yarns (ENF yarns) can form spontaneously during fabrication due to the unique spinning principle, mirroring the structural benefits of CNT yarns.[22] As one of the typical ENF yarn production methods, bath electrospinning collects drafted nanofibers in a liquid medium, facilitating the integration of functional components through nanoassembly during the spinning process.[23] For example, Qin et al. developed CNT/PEDOT:PSS NF yarns with embedded thermoelectric materials, outperforming surface-coated alternatives.[24] However, the application of ENF yarn on TEGs has received limited attention, which is mainly attributed to the fact that hydrophilic polymer nanofibers are prone to cause swelling-induced structural changes. The performance instability caused by structural deformation remains an urgent problem that TEGs need to solve.[25]

Inspired by the nanoassembly strategy of bath electrospinning, a hybrid yarn combining nanofibers and nanosheets was initially fabricated. These components mixed uniformly at nanoscale and aligned orderly along the twisting axis, biomimicking the vascular bundle channel. Subsequent functional processing yielded anti-swelling hybrid yarns with 1D oriented nanoscale channels and satisfied mechanical property, allowing for knotting and weaving. When applied in TEG, a single 4-cm-long yarn could generate stable output of 295 mV and 1.82 μA in a water environment, rising to 360.4 mV and 2.57 μA under simulated perspiration condition. Further, a fabric incorporating sixty 2-cm-long yarns via series-parallel connections achieved the output of 1.85 V, 17.32 μA and 31.96 μW, sufficient to power small electronic devices such as lamp bead and display. The demonstration of our displayed fabric, which can be worn on the human body and generate electricity via liquid-driven method, provides a novel solution for the development of self-powered textiles and highlights a strong potential for wearable intelligent applications.

2. Results and Discussion

2.1. Design and Fabrication of Nanofiber/Nanosheet Hybrid Yarn

We employed the nanoassembly strategy of bath electrospinning to prepare nanofiber/nanosheet hybrid yarn for biomimicking the water transporting mechanism of vascular bundle in *Neottopteris antiqua* (**Figure 1a**). During the spinning process, polymer solution was initially drawn into jet by electric field. Subsequently, it was stretched into nanofiber and deposited in the bath containing nanosheets. At this stage, due to the nanoassembly effect induced by electrostatic attraction and intermolecular hydrogen bonding, nanofibers and nanosheets were able to directly contact and actively adhere to each other, resulting in an even mixing at nanoscale. Afterward, by rotationally pulling out the mixture, a 1D nanofiber/nanosheet hybrid yarn was constructed. Notably, the winding speed influenced the force of pulling the mixture. A large pulling strength compelled the nanofibers and nanosheets to align orderly along the pulling direction.[26] By adjusting the winding speed, nanofibers and nanosheets with an oriented arrangement along the twisting axis could be obtained. Since the gaps between the nanofibers ran along the length direction of the nanofibers, a nanofiber/nanosheet hybrid yarn with 1D oriented channels was implemented. Compared to WS yarn, the channel structure in nanofiber/nanosheet hybrid yarn more closely resembled that of the vascular bundle (Figure 1b). The channels in WS yarn were formed through solvent evaporation and diffusion, which were discrete and arbitrary. Although they may be interconnected, the paths were cumbersome, circuitous, and non-straight-through. Additionally, WS yarn was a fiber with a diameter ranging from tens to hundreds of micrometers. When using the same polymer, more contact opportunities and stronger intermolecular forces could be established between nanofibers and nanosheets, thus enabling more combinations of nanofibers and nanosheets from the inside to the outside (Figure 1c).

To demonstrate that bath electrospinning could be employed to nanoassemble different polymers and nanosheets into yarns, cellulose acetate/polyacrylonitrile (CP), polyacrylonitrile (PAN), polyvinylidene fluoride (PVDF), polypropylene (PS), graphene oxide (GO) and $Ti_3C_2T_x$ carbides (MXene) were selected to construct nanofiber/nanosheet hybrid yarns. These yarns were named CP/GO, PAN/GO, PVDF/GO, PS/GO, CP/MXene, PAN/MXene, PVDF/MXene, and PS/MXene yarns. All these yarns could be wound helically (Figure S1,

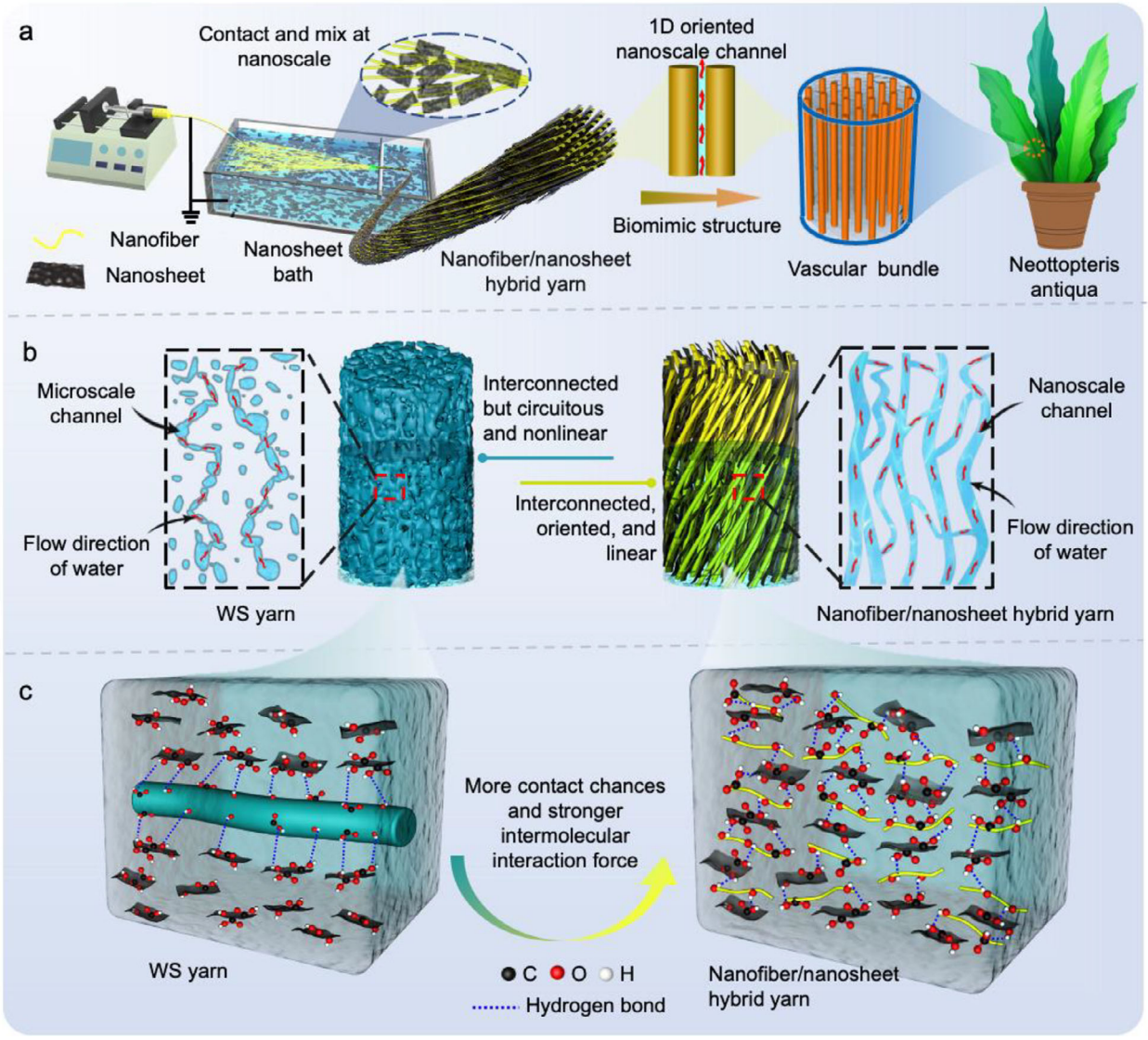

Figure 1. a) Construction mechanism of nanofiber/nanosheet hybrid yarn, b) channel structure and c) fiber/nanosheet contact approach in WS yarn and nanofiber/nanosheet hybrid yarn.

Supporting Information). However, the colors of PS/GO and PS/MXene yarns were slightly lighter than those of other yarns, implying that relatively fewer GO and MXene nanosheets were mixed into these yarns. This phenomenon can be explained by the nanoassembly process that contributed by electrostatic attraction and intermolecular hydrogen bonding. The electrostatic attraction stemmed from the positive charge of nanofibers and the negative charge of collecting bath, which produced by applied electric field during electrospinning, promoting the interfacial contact and homogeneous mixing of various nanofibers and nanosheets. Nevertheless, the strength of electric field weakens or may even be neutralized when nanofibers reach to the bath receiver. As a result, only the directly contacted nanosheets were absorbed to nanofibers. The intermolecular hydrogen bonding derived from in polar nanofibers/nanosheets that containing hydroxyl, amino, or hydrogen fluoride groups, serving as an additionally attractive force between nanofibers and nanosheets, which further contributes to the mixing of adjacent or distanced nanosheets with nanofibers. This viewpoint was confirmed by taking cellulose acetate (CA) and polypropylene (PS) as examples to calculate surface binding energy through first-principle calculations (**Figure 2**a,b). The results revealed that CA had a stronger surface binding energy with GO than PS (Figure 2c). This is because CA contains more hydroxyl groups, which lead to stronger intermolecular hydrogen bonding interaction. Since PS lacks hydroxyl, amino, or hydrogen fluoride groups, relatively fewer nanosheets are mixed into the yarn, causing it to display a relatively lighter color.

Taking CP/GO yarn as an example to characterize the microstructure of hybrid yarn, both the twisted structure and uniform evenness were exhibited (Figure 2d). Nanofibers and nanosheets presented orderly orientation along the twisting axis, forming tight adhesion (Figure 2e). The parallel alignment

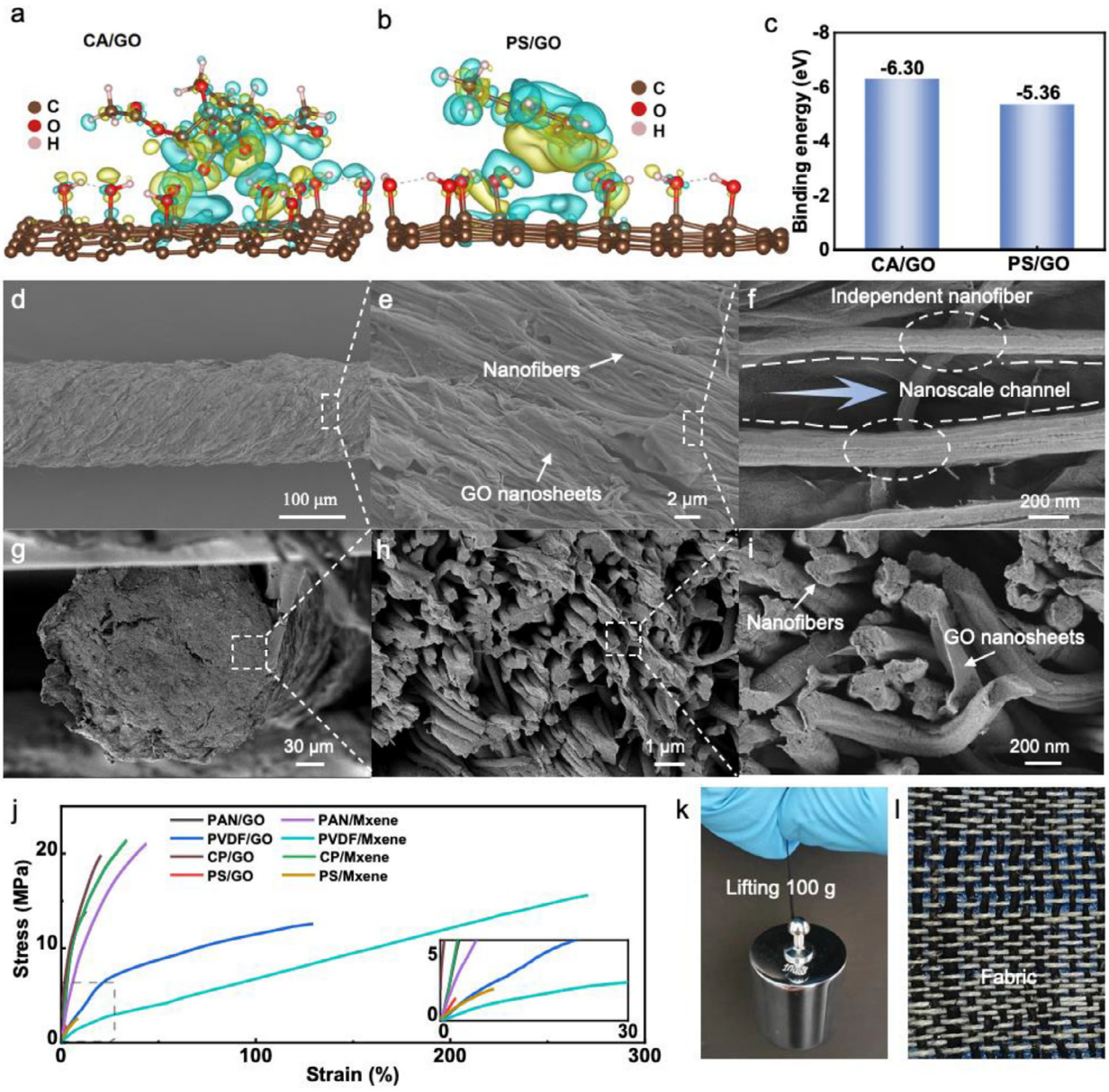

Figure 2. a–c) Surface binding energy of CA and PS with GO, d–f) surface and g–i) cross-section SEM images of CP/GO yarn, j) stress-strain curves of various hybrid yarns, k) a 100 g weight lifted and l) a fabric woven by CP/GO yarns.

created a well-defined 1D oriented channel between adjacent nanofibers (Figure 2f). Moreover, large pieces of GO lied on the surfaces of nanofibers (Figure S2, Supporting Information) and GO nanosheets gradually transitioned from discontinuity to continuity on the nanofiber surfaces as the content of GO nanosheets increased (Figure S3, Supporting Information). To better understand the oriented channel structure, a nanofiber/nanosheet hybrid yarn with poor orientation and randomly distributed nanofibers are displayed in Figure S4 (Supporting Information), which was difficult to observe the oriented arrangement of nanofibers and channels, indicating our viewpoint of oriented inter-fiber channel structure. Furthermore, the cross-sectional SEM image of CP/GO yarn showed a typical cylindrical structure (Figure 2g). Nanofibers and nanosheets were distributed uniformly from the inside to the outside (Figure 2h,i). This structural consistency extended to other nanofiber/nanosheet hybrid yarns (Figure S5, Supporting Information). For comparison, we also prepared two types of CP/GO microyarns by wet spinning, which displayed a significant structural difference compared to CP/GO yarns. No visible pores were observed on the surface of the two WS yarns, but uneven pores could be identified in their cross-sectional images (Figure S6, Supporting Information). This phenomenon was also a typical feature of pores in WS yarns. The stress-strain curves revealed excellent mechanical tensile properties in all nanofiber/nanosheet hybrid yarns except PS/GO and PS/MXene (Figure 2j). This may be attributed to the relatively low nanosheet loading in the two yarns. The inferior mechanical

performance of pure ENF yarns further confirmed the critical role of nanosheets in mechanical reinforcement (Figure S7, Supporting Information). Additionally, we characterized the stress-strain behavior of poorly oriented CP/GO yarn to elucidate the impact of orientation on mechanical property (Figure S8, Supporting Information). The highly oriented CP/GO yarn exhibited improved stress and strain, attributable to parallel-aligned nanofibers and nanosheet that enhance the utilization of fiber/sheet strength while reducing stress defects caused by fiber/sheet bending. Furthermore, bending stiffness and friction coefficient across orientation variants were also measured to confirm weaving ability (Figure S9, Supporting Information). Both yarns exhibited bending stiffness and friction coefficient comparable to common woven yarns. However, the highly oriented yarn showed increased bending stiffness and reduced friction coefficient compared with its poorly oriented counterpart, which correlated to twist-induced structural consolidation and surface smoothing. To visually demonstrate the mechanical usability, CP/GO yarns were selected to lift a 100 g weight and woven into a fabric (Figure 2k,l), showcasing remarkable textile integration potential.

2.2. Functional Processing

Given the importance of medium feature, channel structure, and water anti-swelling ability for TEG, the closed water-based isocyanate (BIC) doped CP/GO yarns (labeled as CGB yarn) were chosen for subsequent functional processing to build wearable TEGs. CGB yarn underwent initial deacetylation to promote CA hydrolysis, followed by heat treatment at 120 °C to establish chemical crosslinking (**Figure 3a**). Deacetylation was used to increase hydroxyl group density of CP nanofiber surfaces by replacing ester groups with hydroxyl groups, where heating facilitated BIC-mediated isocyanate exposure, and enabled polyurethane reaction between isocyanate and hydroxyl groups to generate carbamate and achieve nanofiber crosslinking at contact points. FTIR results could clearly demonstrate the chemical changes in these two stages (Figure S10, Supporting Information). The disappearance of absorption peaks at ≈1751 and ≈1246 cm^{-1} represented the process of replaced ester groups. The deacetylated CGB yarn (labeled as dCGB) heated for 5 min revealed a prominent enhancement of the ≈2252 cm^{-1} peak and a weak stage of the ≈1740 cm^{-1} peak, corresponding to isocyanate exposure and the preliminary generated carbamate. Persistent heating for 25 min resulted in a significant weakening of the ≈2252 cm^{-1} peak and a stable maintenance of ≈1740 cm^{-1} peak, confirming thorough hydroxyl-isocyanate reactions for generating carbamate. Notably, the FTIR result of CGB yarn clearly revealed the ester group peak of CA at ≈1246 cm^{-1} and the nitrile group peak of PAN at ≈2252 cm^{-1}. However, the characteristic peak for BIC could not be definitively identified. Because the isocyanate groups in BIC were blocked prior to heating and prevented appearance of the peak at ≈2270 cm^{-1}. Additionally, the C═O and N—H signals from BIC overlapped with the C═O and O—H groups of CA.

Crosslinked dCGB yarn (labeled as CdCGB) retained the desired yarn structure and ordered fiber arrangement (Figure S11, Supporting Information). Essentially 1D oriented nanoscale channel between nanofibers was also preserved (Figure 3b,c). Meanwhile, crosslinking feature could be observed at fiber contact points, though excessive BIC content caused nanofiber fusion rather than discrete crosslinking (Figure S12, Supporting Information), contrasting with the independence in BIC-free yarn (Figure 2f). In addition, nano-computed tomography (nano-CT) and channel size distribution of CdCGB yarn were further characterized to reveal the channel characteristics. Blue color in the nano-CT image represented the internal channels of CdCGB yarn, which clearly displayed the 1D oriented and continuous channel structure (Figure 3d; Figure S13, Supporting Information). Channel size ranged from a few nanometers to 10 µm and predominantly centered below 1000 nm (Figure 3e). This contrasted with the channel distribution exceeding 1000 nm observed in CP/GO microyarns. Furthermore, the negatively charged channels could also be discovered in CdCGB yarn through Zeta potential (Figure 3f), granting the possibility of EDL formation. The enhancement of Zeta potential for dCGB and CdCGB yarns is mainly due to the increase of charged hydroxyl groups after deacetylation. The changes in water contact angle were explained as deacetylation reduced water contact angles through hydroxyl group generation, while subsequent heating slightly reversed this trend through GO reduction (Figure 3g). Besides, CdCGB yarn demonstrated exceptional water anti-swelling ability, maintaining an undamaged structure after 10-day water immersion, whereas dCGB yarn showed visible swelling within 2 h (Figure S14, Supporting Information). The swelling ratios of dCGB and CdCGB yarns soaked in water for 48 h were 231% and 0.7%, respectively, while after 10-day of immersion in water CdCGB yarn just showed a negligible increase in swelling ratio of 0.6% (Figure 3h). Moreover, similar anti-swelling ability persisted in sodium chloride (NaCl) solution. This stability originated from the crosslinked network encapsulating GO nanosheets to restrict expansion and complemented by hydrophobic microenvironments at crosslinking points formed through isocyanate-hydroxyl reactions. The localized hydrophobic regions not only repelled water molecules but also optimized channel dimensions and ion selectivity.[27] In contrast, water infiltration disrupted hydrogen bonding in dCGB yarn, thus causing structural expansion. After immersion and drying, the SEM images revealed the collapsed structure of dCGB yarn, whereas CdCGB yarn preserved a circular morphology (Figure S15, Supporting Information). Emphatically, CdCGB yarn retained excellent mechanical properties after functional processing, with a breaking stress of 26.83 MPa and a breaking strain of 17.82%, which increased 35.2% in stress and decreased 12.9% in strain compared to CP/GO yarn (Figure 3i). The changes in mechanical properties can be explained as applied forces being more evenly dispersed throughout the yarn through cross-linking points, thereby reducing local stress concentration. Concurrently, the increase in rigidity also led to a reduction in elastic deformation under the same load. The bending stiffness and frictional coefficient of CdCGB yarn were also tested to indicate the preservation of weaving ability. Both parameters remained satisfactory results, with bending stiffness at 0.28 and frictional coefficient at 0.29 $cN \times mm^2$ (Figure S9, Supporting Information). Superior mechanical properties allow CdCGB yarns to be softly knotted and easily integrated into fabrics (Figure 3j). Considering that CdCGB yarns used in TEGs could not be woven in common patterns, we wove them into a formed fabric based on the pattern of end separation to confirm their textile

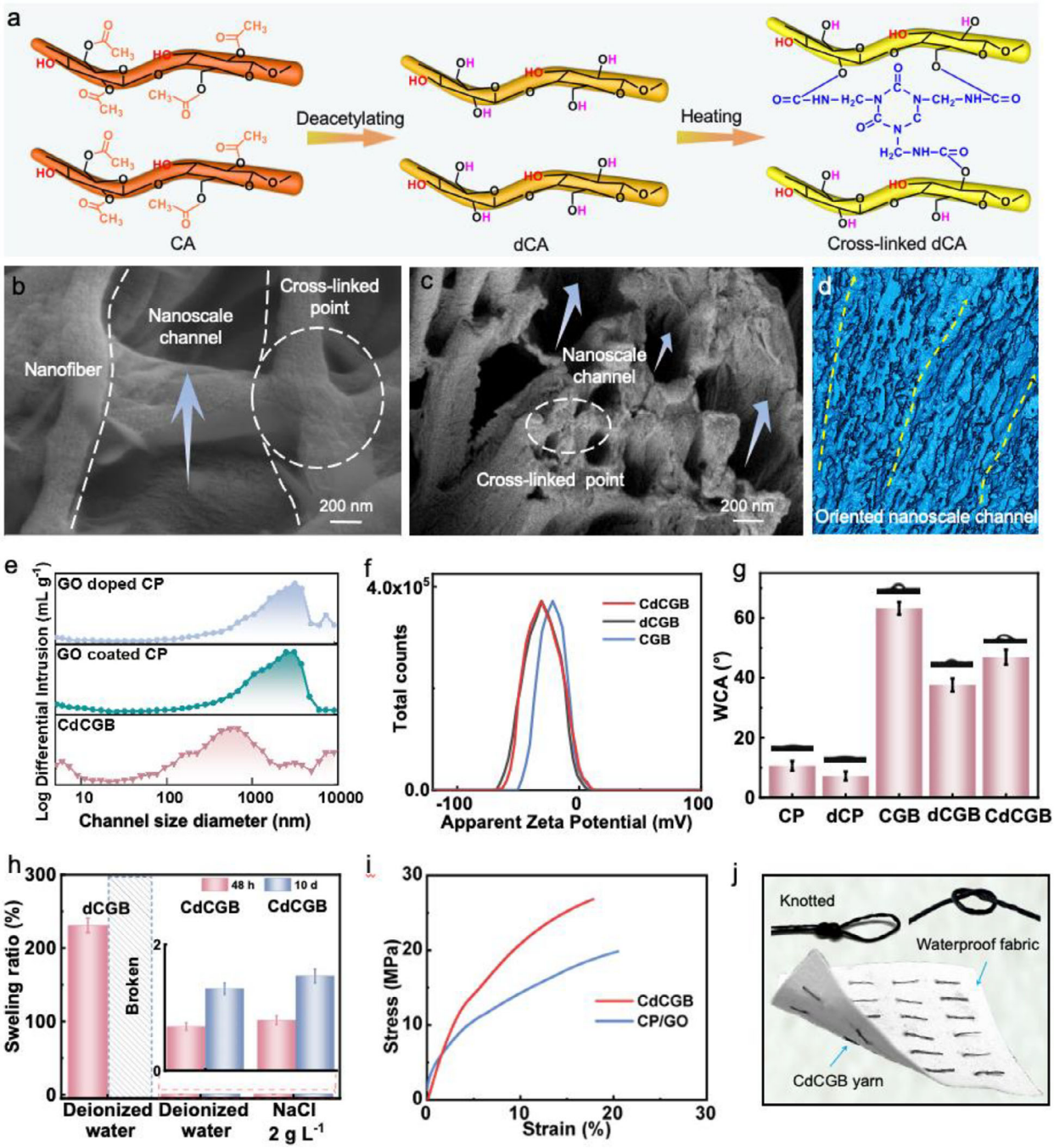

Figure 3. a) Functional processing of CGB yarns, b,c) SEM images, d) nano-CT image, e) channel size distribution, f) Zeta potential, g) water contact angle, h) anti-swelling ability, i) Stress-strain curves and j) visual display of mechanical properties.

compatibility, further directly using for the subsequent demonstration of wearable application.

2.3. Output Electrical Performance

When an electrolyte flows through a capillary channel with a charged surface, an EDL can form within the channel, inducing ions to accumulate downstream and generate a flow potential.[28] Guided by this principle, the output power of a TEG based on a 4-cm-long CdCGB yarn was measured under the ambient conditions of 45% RH and 25 °C by immersing one end of CdCGB yarn in deionized water while exposing the other end to air (**Figure** 4a and Movie S1, Supporting Information). As water evaporated, the output voltage and current gradually increased from baseline until stabilizing at 295 mV and 1.82 µA, respectively (Figure 4b,c). Subsequent steady-state measurements of open-circuit voltage (*Voc*) and short-circuit current (*Isc*) yielded results consistent with

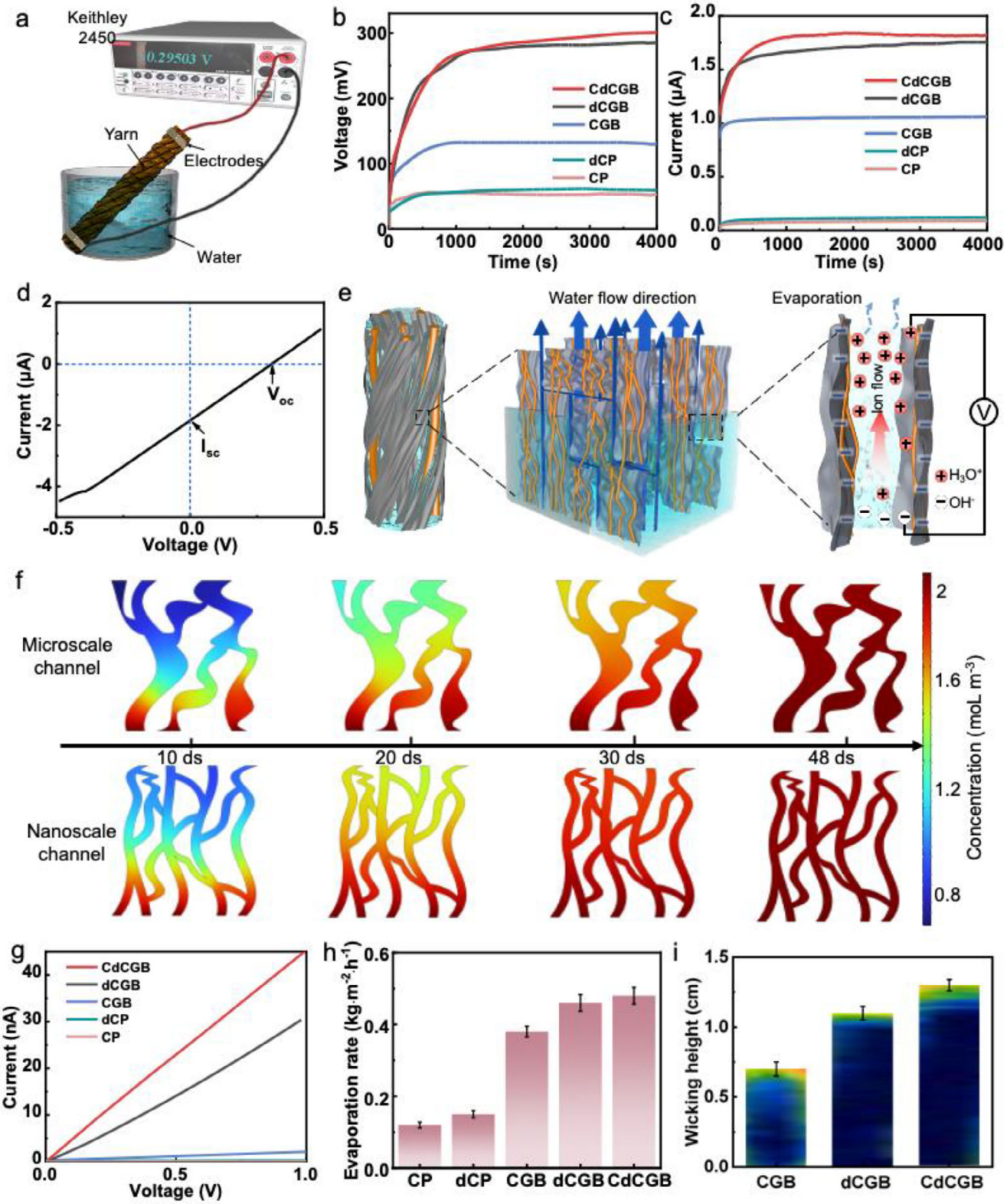

Figure 4. a) Schematic diagram for testing TEG output power, b) voltage and c) current of TEGs based on different yarns, d) *I-V* curve of TEG based on CdCGB yarn under steady-state, e) mechanism diagram of TEG based on CdCGB yarn, f) water concentration distributions obtained by finite element simulation in both of microscale channels and nanoscale channels along the time span of 10 to 48 ds, g) conductivity, h) evaporation rate and i) wicking height of TEGs based on CGB, dCGB and CdCGB yarns.

the time-dependent voltage (*V-t*) and current (*I-t*) (Figure 4d). To confirm the transpiration-driven power generation of CdCGB yarn-based TEG, the voltage output was monitored while alternating between opened and closed container configurations (Figure S16, Supporting Information). Opening the container induced a gradually increased voltage until equilibrium was reached. Subsequent closure caused voltage decay as vapor saturation inhibited evaporation, while reopening restored voltage recovery. This behavior aligns with the mechanism whereby transpiration-driven water flow through negatively charged nanoscale channels generates directional ion migration (Figure 4e). When the size of the channel is smaller than or equal to the Debye length of water (≈980 nm), the EDL will overlap with the channel containing hydrolyzed cations or anions, thus enhancing ion selectivity by suppressing random diffusion.[29] In this situation, the surface charge dominates the ion transport mechanism, which can effectively enhance the formation of the unidirectional counteracting ion (H_3O^+) stream with high concentration toward the yarn's air-exposed end, while repelling co-ions (OH^-) accumulate at the submerged end. This charge separation creates a sustained flow potential and current. In contrast, larger channels exceeding 980 nm, such as two types of CP/GO microyarns, cannot permit EDL overlap in the central area, which was not conducive to ion-selective migration (Figure S17, Supporting Information). Besides, the tortuous and nonlinear channel pathway adversely affects water transport dynamics, which diminishes the electrical output capability. The theoretical investigation of water transport behavior in macroyarns with varying interconnection channel numbers, supported by finite element simulations, revealed critical insights into the role of interconnectivity. Simplified 2D models, consisting of microscale/nanoscale channels with and without interconnections, were employed to study water concentration profiles over time. Figure 4f illustrates the striking differences in water transport efficiency between the two configurations, even within a short time span of 48 ds. Microscale channels lacking interconnections exhibited severely diminished water mass transfer, attributed to the discontinuity in diffusion pathways. This reduction in interconnection disrupted the continuity of water transport, significantly hindering the overall diffusion process. In stark contrast, nanoscale channels featuring multiple interconnections demonstrated highly efficient water transport. The enhanced connectivity provided continuous diffusion passages, facilitating a more uniform and effective mass transfer of water molecules across the structure. The above analysis suggested that the interconnection effectively enhances the water transport, further contributing to larger power generation in CdCGB yarn.

The electrical output performances of TEGs utilizing various ENF yarn substrates were systematically investigated. CP and dCP yarns exhibited reduced output voltages and currents owing to their electrical insulation (Figure 4g). Poor conductivity directly impacts charge transfer efficiency.[30] CdCGB yarn exhibited improved conductivity due to partial GO reduction during deacetylation and heating, which was evidenced by an increased D/G band intensity ratio from 0.96 to 1.008 (Figure S18, Supporting Information). The incorporation of GO nanosheets in CGB yarn substantially improved both voltage and current outputs through enhanced water evaporation (Figure 4h). Inadequate evaporation restricts ionic migration,[31] while the increase in evaporation rate can be attributed to the enhanced light absorption of black GO. Subsequent deacetylation further boosted electrical output, potentially through synergistic enhancements in wicking height (Figure 4i), Zeta potential, conductivity, and evaporation. Elevated Zeta potential modifies the effect of EDL.[29] Higher Zeta potential indicates the larger surface charge density of the yarn, which can transfer more charges and form a thicker EDL and ion concentration, thereby enhancing the energy conversion efficiency. While increased wicking height enhances water transport.[32] Notably, although the water contact angle of CdCGB yarn was 9.3° higher than that of dCGB yarn, its wicking height was superior. The reason for this unusual rule may be that the cross-linked fiber structure promotes water transport more effectively than the insignificant difference in water contact angle. Further heating marginally improved the outputs, mainly because cross-linked network facilitated water absorption along hydrophilic nanofibers.

The power generation of CdCGB yarn under different deacetylation parameters (NaOH concentration and treating time) were also tested considering that it might be affected by hydrophilicity, conductivity, and surface potential. All the data regarding these factors were collected at steady state. As NaOH concentration increased, the output voltage initially increased and then decreased, whereas the current gradually increased (**Figure 5**a). This was mainly because a high NaOH concentration was beneficial for enhancing the hydrolysis of CA and the reduction of GO, thus improving the conductivity and hydrophilicity of the yarn (Figure S19, Supporting Information). However, an excessive NaOH concentration led to an increase in the degree of GO reduction and a decrease in resistance, causing the voltage to drop. As the treating time prolonged, the output electrical performance followed a similar trend to that of the NaOH concentration (Figure 5b; Figure S20, Supporting Information). With an increase in the content of GO nanosheets, the output voltage and current improved due to enhanced conductivity (Figure 5c; Figure S21a, Supporting Information). When the content of GO nanosheets was too high, the proportion of nanofibers in CdCGB yarn decreased, which led to a reduction in hydrophilicity (Figure S21b, Supporting Information), thereby impeding the absorption and transportation of water. In addition, as the length of CdCGB yarn increased, both the voltage and current went up because of the larger evaporation area (Figure 5d). Moreover, the external environment, including ambient temperature and air-flow velocity, had an impact on power generation. Increasing ambient temperature and air-flow velocity was beneficial for improving the output electrical performance (Figure 5e,f), as high ambient temperature and air-flow velocity could increase the evaporation rate. The output electrical performances of CdCGB yarn in different liquids were also tested (Figure 5g). When the ion concentration increased to 2 g L^{-1} (similar to sweet), the output voltage and current reached to 360.4 mV and 2.57 μA, respectively. This was because the net charge (σ) increased with the increase of ion concentration.[33] For similar materials or structures, CdCGB yarn exhibited more excellent power generation capability (Figure S22, Supporting Information). When CdCGB yarn was placed in a testing device with sufficient water, a stable output voltage could be maintained for up to 60 h (Figure 5h). By gradually increasing the resistors, the voltage across the load gradually increased, while the current gradually decreased (Figure 5i). The

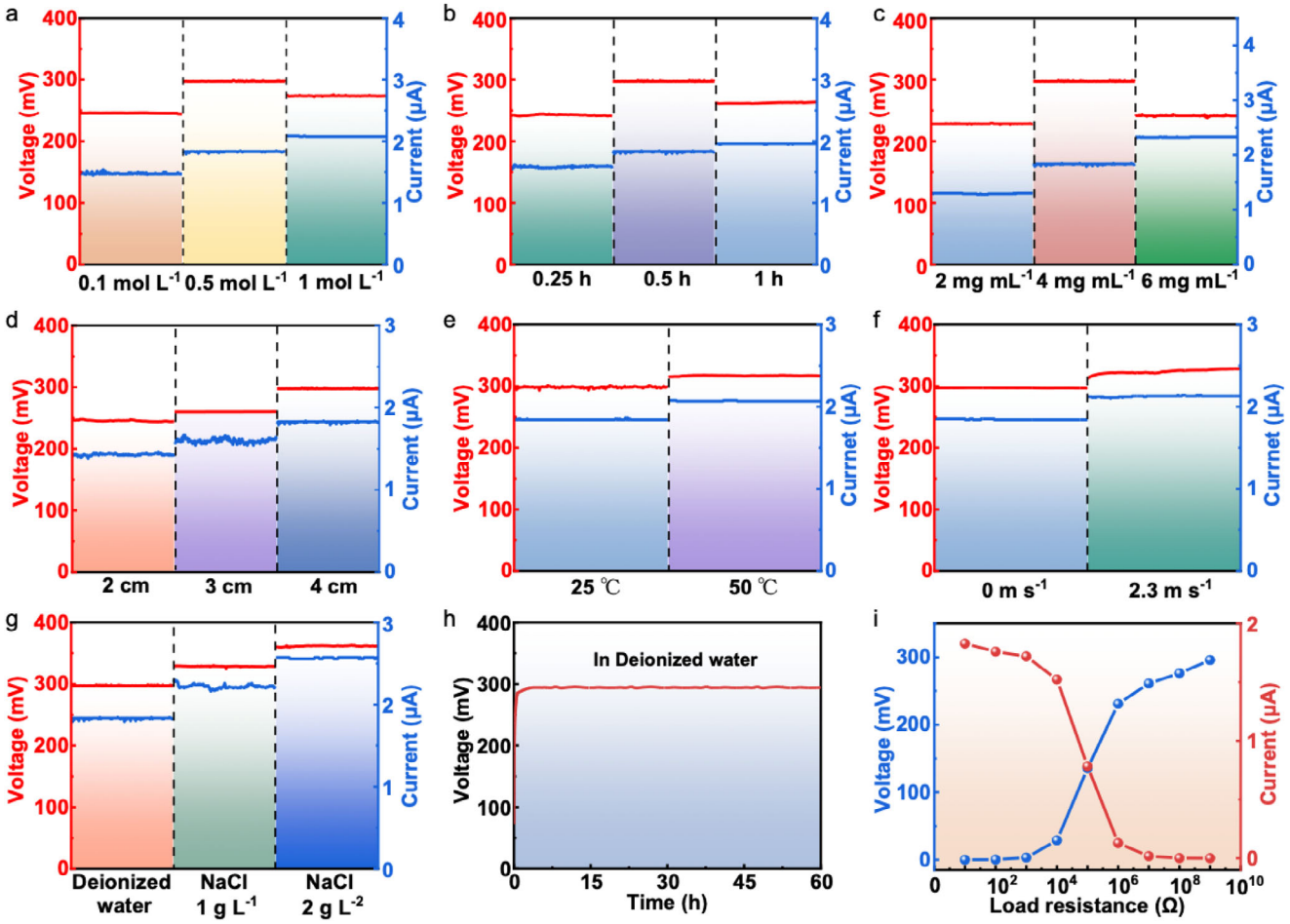

Figure 5. Output voltage and current of TEG based on CdCGB yarn under different a) NaOH concentrations, b) treating time, c) GO nanosheet content, d) yarn length, e) ambient temperature, f) air flow velocity, and g) liquid environment, h) stability of output voltage, i) output voltage and current as a function of external resistance.

maximum output power was ≈106 nW (Figure S23, Supporting Information).

2.4. Wearable Application

Considering the practical application in wearable products, the electrical performance of CdCGB yarn was further tested by continuously supplying a fixed-volume droplet (0.5 mL) onto one end of the yarn (**Figure 6**a and Movie S2, Supporting Information). The TEG based on CdCGB yarn was able to continuously generate an electrical signal with a voltage of 322 mV and a current of 1.74 μA, which was similar to the result of the immersing test (Figure 6b,c). The maximum output power was 560.28 nW (Figure S24, Supporting Information). During the repeated process of water supply and evaporation, a periodic rising and falling of the voltage can be observed, which demonstrates its stable electrical output ability and good reusability (Figure 6d). Furthermore, the output electrical ability could be further improved by connecting four CdCGB yarns in series and parallel (Figure 6e,f). When six CdCGB yarns were connected in series, a capacitor could be charged to 1.58 V in 12 000s, which was significantly higher than that of a single CdCGB yarn within the same time (Figure 6g). In addition, due to the requirement of a humidity gradient in TEG, yarns cannot be woven into fabrics in a common method, as it is necessary to have one wet end and one dry end. As a conceptual demonstration, we proposed a double-layer fabric design that could perfectly achieve independent control of the wet and dry ends of the yarn (Figure S25, Supporting Information). However, to simplify the manufacturing process, we wove CdCGB yarns into a single-layer fabric with excellent waterproof performance for demonstrating wearable application through using a series-parallel connection method (Figure S26, Supporting Information). The two ends of the yarn were placed on both sides of the fabric, with one side in contact with droplets and the other side exposed to the air. Due to the barrier of the waterproof fabric and the induction of evaporation, the liquid would be transported longitudinally along the yarn from one end to the other (Figure 6h). When simulated sweat (a NaCl solution with a concentration of 2 g L^{-1}) was continuously inputted, a voltage of 1.85 V, a current of 17.32 μA and a power of 31.96 μW could be generated (Figure 6i; Figure S27, Supporting Information). A small lamp bead was easily illuminated by using this fabric (Figure 6j and Movie S3, Supporting Information). Moreover,

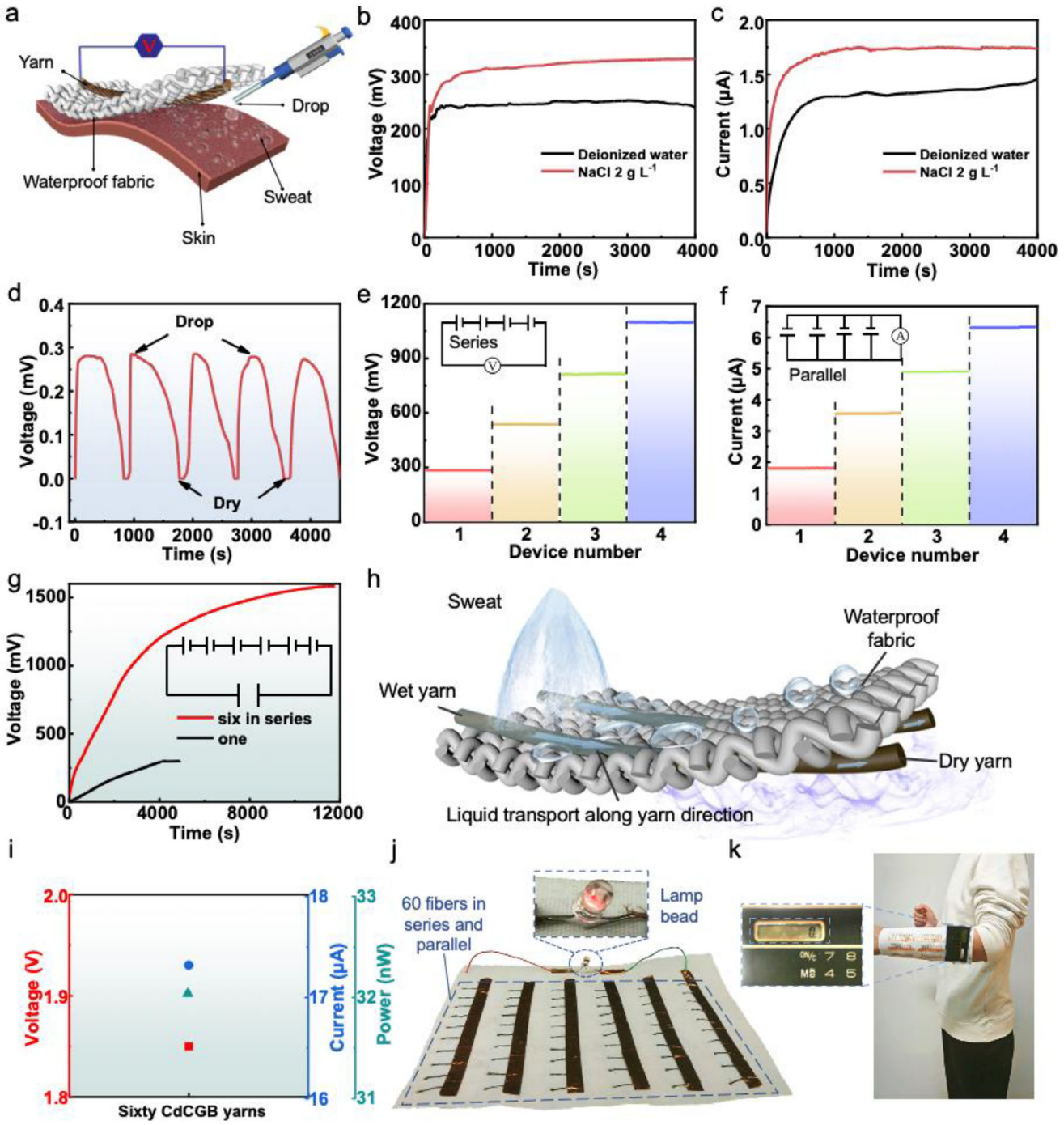

Figure 6. a) Schematic diagram of dripping test, b) voltage and c) current of TEG based on CdCGB yarn in different liquids (yarn length was 2 cm), d) voltage under repeated dripping and evaporation process, e) voltage of four CdCGB yarns in series, f) current of four CdCGB yarns in parallel, g) *V-t* curves when charging a capacitor, h) working principle diagram of CdCGB yarns woven into textile, i) average voltage, current and power of sixty CdCGB yarns, sixty CdCGB yarns woven into a waterproof fabric to power small, j) lamp bead and k) display screen.

to present the concept of wearables more clearly, we made this fabric into a sleeve and wore it on the volunteer's arm. When the yarns were wetted in advance to simulate human sweating, a small electronic display screen was successfully powered by the worn sleeve (Figure 6k and Movie S4, Supporting Information), fully demonstrating its potential for wearable application.

3. Conclusion

In this work, CdCGB yarn was constructed via bath electrospinning followed by a functionalization process. GO nanosheets were in full contact with CP nanofibers within the yarn and uniformly mixed from the interior to the exterior, endowing CdCGB

yarn with excellent 1D oriented nanoscale channel structure. Moreover, CdCGB yarn exhibited remarkable surface charge, conductivity, weaving ability and water anti-swelling property, achieving an intact structure even after being soaked in water for 10 days. When employed in TEG, a single CdCGB yarn could generate a stable output voltage for up to 60 h. The output voltage and current reached 295 mV and 1.82 μA, respectively. In a simulated sweat liquid environment, an output voltage of 360.4 mV and an output current of 2.57 μA could be achieved. Furthermore, by weaving sixty CdCGB yarns into a waterproof fabric through series-parallel connection, an output voltage of 1.85 V, an output current of 17.32 μA and an output power of 31.96 μW were attained. This fabric could power a lamp bead and a small electronic display successfully, indicating its outstanding application potential in wearable field.

4. Experimental Section

Materials: Cellulose acetate (CA, Mw 50, 000), polyacrylonitrile (PAN, Mw 1, 000, 000), polyvinylidene fluoride (PVDF, Mw 600000) and polystyrene (PS, Mw 60, 000) were purchased from China National Chemical Reagent Co., Ltd. N-N-dimethylformamide (DMF, 99.8%), tetrahydrofuran (THF, AR), sodium hydroxide (NaOH, AR), and anhydrous ethanol (AR) were purchased from Shanghai Aladdin Reagent Co., Ltd. The closed water-based isocyanate (BIC, H1003) was purchased from Guangzhou Hengshuike New Materials Co., Ltd. Graphene oxide dispersion (GO, 2–10 mg mL^{-1}, solvent ethanol) was purchased from Suzhou Carbon Feng Graphene Technology Co., Ltd. MXene dispersion (MXene, 4 mg mL^{-1}, solvent ethanol) was purchased from Shandong Enyan New material Technology Co., Ltd. Waterproof fabric (polyester, yarn count 45 × 45, fabric density 96 × 72) was purchased from Zhejiang Xinyu Textile Co., Ltd.

Preparation of Nanofiber/Nanosheet Hybrid Yarn: During the electrospinning process, polymer solution was first drawn into jet and then stretched into nanofiber by electric field. Formed nanofibers were deposited in the bath containing nanosheets to generate a nanofiber/nanosheet mixture. By further rotationally pulling out the mixture, a nanofiber/nanosheet hybrid yarn was obtained. Finally, the end of the continuously extracted hybrid yarn was brought into contact with the rotating winding roller, and the orientation of the nanofibers and nanosheets was controlled by adjusting the winding speed. To increase the spinnability, the CP mixture composed of CA and PAN was selected as the spinning polymer. CP solution (wt.% 15%) was prepared by sequentially adding CA and PAN in a mass ratio of 8:2 to DMF solvent and stirring at room temperature for 6 h. The concentration of PAN, PVDF, and PS solution were 15%, 9%, and 15%, respectively. The spinning parameters, including a voltage of 20 kV, a distance of 15 cm between the needle and the bath, a solution flow of 1.5 mL h^{-1}, a winding speed of 20 cm/min, a relative humidity of 50% ± 5%, and a temperature of 25 °C ± 5 °C, were selected. Pure NF yarns were obtained through a bath without nanosheets.

Preparation of Functionalized Yarn: BIC-doped CP solution was prepared by adding BIC (10–30% of CA weight) in CP solution and magnetic stirring for 2 h, and then used to fabricate CGB yarns. CGB yarn was immersed in NaOH solution (0.1–1 mol L^{-1}) for 0.1–1 h to obtain dCGB yarn. NaOH solution was prepared by dissolving NaOH powders in a mixture of ethanol/deionized water with a volume ratio of 2:1 and stirring for 0.5 h. The dCGB yarn was heated at 120 °C in an oven for 0.5 h to obtain CdCGB yarn. In addition, CP, dCP, CP/GO, and dCP/GO yarns were functionally processed by the same parameters.

Construction of Yarn-Based TEGs: Two copper foils were first pasted on the upper and lower ends (distance of 3 cm) of a supporting substrate to serve as electrodes. Conductive tapes were then used to fix both ends of a 4-cm-long yarn onto the copper foil surfaces while simultaneously connecting wires to each terminal, thereby completing the assembly of a single-yarn-based TEG. During immersion testing, the TEG was positioned at an angle within a water-filled container, with the water height maintained at half the length of yarn. For the dripping evaluation, controlled water droplets were directly released onto the yarn at one end of a horizontal TEG. Yarn-integrated wearable TEG was obtained by weaving the yarn up and down in a waterproof fabric, ensuring terminal placement on opposing fabric surfaces. These yarn ends were then affixed using flexible conductive tapes with integrated conductive wires. The electrical output performance of yarn-integrated TEG was tested by supplying liquid on one side of the waterproof fabric.

Characterization: Morphology was observed by ZEISS Ultra 55 (Zeiss, Germany). Nano-CT image was characterized by ZEISS Xradia520 (ZEISS, Germany). Strain-stress property was tested by Instron 5969 (INSTRON, UK) with a sample length of 50 mm and a testing speed of 100 mm min^{-1}. Chemical structure and composition were characterized by Nicolet iS 50 (FTIR, Thermo Fisher Scientific, USA) and Horiba Scientific (Raman, HORIBA France SAS, USA). Pore size distribution was characterized by AutoPore V 9600 (Micromeritics USA). Zeta potential was tested by Malvern Zetasizer Nano ZS90 (Malvern, UK). Water contact angle was conducted by OCP20 (Dataphysics, Germany). The swelling ratio was calculated by testing the diameter change of the yarn before and after soaking in water. Bending stiffness and frictional coefficient were tested through combining Instron 5969 (INSTRON, UK) with self-made devices (Figure S28, Supporting Information). Voltage, resistance, and current were recorded by Keithley 2450 (Keithley, USA). Water evaporation rate was determined by calculating the ratio of weight difference (before and after soaking in water) to the product of surface area and evaporation time. Wicking property was exhibited by wicking height, which was characterized by analyzing color difference in the image (record by FOTRIC 320Q, Shanghai Thermal Imaging, China) of dried yarn vertically inserting into water for 10 min. The moistened segments of the yarn exhibited lower temperatures compared to the dry regions. Infrared thermal imaging systems could distinctly capture this temperature variation through chromatic differentiation, where disparate heat levels were represented by varying color gradients.

Finite Element Simulation: The water transport in hybrid microyarn with and without interconnections, 2D models of hybrid microyarn were constructed. The channel model used in the finite element simulations in Figure 4f is established based on the SEM-observed structure and channel size distribution in Figure 3e and Figure S6 (Supporting Information) and Figure 3c. Specially, the channel size of GO-doped CP and GO-coated CP prepared by wet spinning were primarily distributed in the range of 1–10 μm. In contrast, CdCGB yarn exhibits channel size distributed within 100 nm to 1 μm, as well as in the sub-10 nm range. Moreover, most of the channels in CdCGB sample are clearly interconnected in Figure 3c, whereas the channels in the GO-doped CP and GO-coated CP samples in Figure S6 (Supporting Information) were largely isolated and not interconnected. The mass transfer process in the hybrid microyarn can be described by:[34]

$$\rho\nabla \cdot u = \nabla \cdot [-pI + K] + F \quad (1)$$

$$\rho\nabla \cdot u = 0 \quad (2)$$

$$K = \mu(\nabla u + (\nabla u)T) \quad (3)$$

where ρ represents the mass density, $\boldsymbol{u}$ is the velocity vector, p is the pressure, $\boldsymbol{I}$ is the second-order unit tensor, $\boldsymbol{K}$ is the viscous stress tensor, $\boldsymbol{F}$ is the gravity of water, $\boldsymbol{u}$ is the viscosity of water, T is the temperature of water.

The first principle calculation were performed using density function theory (DFT) as implemented in the Vienna ab initio simulation package (VASP).[35] The interaction between ionic cores and valence electrons[36] was described using the projector augmented wave (PAW) method. The exchange-correlation functional was treated with the generalized gradient approximation (GGA) in the Perdew-Burke-Ernzerhof.[37,38] A plane-wave basis set with a cutoff energy of 500 eV was employed to ensure the accuracy of calculations. Structural optimizations for CP/GO and PS/GO systems were performed using a 3 × 3 × 1 k-point mesh to sample the Brillouin zone of the adsorption structures. The self-consistent iterative

loop convergence criterion was 10^{-6} eV in electronic relaxation and all the atoms were fully relaxed until the force on each atom is less than 0.02 eV $Å^{-1}$.

Supporting Information

Supporting Information is available from the Wiley Online Library or from the author.

Acknowledgements

This work was supported by the National Natural Science Foundation of China (No. 52376063), the Key Research Projects of Higher Education Institutions in Henan Province (No. 24A54005), the High-level Talent Internationalization Funding Project of Henan Province, the Youth Backbone Teacher Project of ZUT (No. 2024XQG05), the Research Institute for Intelligent Wearable Systems of the Hong Kong Polytechnic University (No. P0053074) and the Research Centre of Textiles for Future Fashion of the Hong Kong Polytechnic University (No. P0051306).

Conflict of Interest

The authors declare no conflict of interest.

Data Availability Statement

The data that support the findings of this study are available from the corresponding author upon reasonable request.

Keywords

1D oriented nanoscale channel, nanoassembly strategy, nanofiber/graphene hybrid yarn, wearable transpiration-induced electrical generator, water anti-swelling capability

Received: April 29, 2025
Revised: June 9, 2025
Published online: July 4, 2025

[1] W. Gao, M. Yu, L. Cao, P. W. Yi, S. J., Ren, S. Ling, *Nano Lett.* **2025**, *25*, 2396.
[2] K. Mao, Y. Zhang, S. C. Tan, *Nat. Water* **2025**, *3*, 144.
[3] Y. Hu, W. Yang, W. Wei, Z. Sun, B. Wu, K. Li, Y. Li, Q. Zhang, R. Xiao, C. Hou, H. Wang, *Sci. Adv.* **2024**, *10*, adk4620.
[4] L. Wang, M. Xia, L. Li, Y. Wu, Q. Cheng, J. Xu, S. He, K. Liu, D. Wang, *J. Colloid Interface Sci.* **2024**, *674*, 1019.
[5] Y. Xu, P. Chen, J. Zhang, S. Xie, F. Wan, J. Deng, X. Cheng, Y. Hu, M. Liao, B. Wang, X. Sun, H. Peng, *Angew. Chem. Int. Ed.* **2017**, *56*, 12940.
[6] J. Chen, Y. Li, Y. Zhang, D. Ye, C. Lei, K. Wu, Q. Fu, *Adv. Funct. Mater.* **2022**, *32*, 2203666
[7] Y. Liang, F. Zhao, Z. Cheng, Q. Zhou, H. Shao, L. Jiang, L. Qu, *Nano Energy* **2017**, *32*, 329.
[8] J. Xie, Y. He, J. Qi, Q. Chen, *Polym. Test.* **2024**, *133*, 108391.
[9] P. Wang, J. Gao, B. Xiao, G. Long, Q. Zheng, D. Shou, *Langmuir* **2024**, *40*, 9741.
[10] H. Li, H. Cheng, B. Wu, W. Wang, Y. Zhang, J. Han, *Chem. Eng. J.* **2024**, *495*, 153497.
[11] J. Lan, W. Hong, H. Li, S. Wang, C. Dong, Y. Li, *Desalination* **2024**, *580*, 117545.
[12] J. Guo, L. Zhang, C. Zhang, D. Zhong, W. Long, J. Qin, Z. Fu, S. Zhou, J. Gong, H. Pan, H. Ji, L. Du, L. Xia, *Chem. Eng. J.* **2024**, *496*, 154167.
[13] J. C. Feng, S. X. Li, Z. P. Zhang, Y. An, Q. S. Gao, Z. Sun, H. Xia, *Nano Energy* **2024**, *119*, 109103.
[14] Z. Gui, Z. Yang, D. Xiang, *Chem. Eng. J.* **2024**, *494*, 153010.
[15] K. H. Lee, D. J. Kang, W. Eom, H. Lee, T. H. Han, *Chem. Eng. J.* **2022**, *430*, 132759.
[16] Z. Liu, K. Zheng, L. Hu, J. Liu, C. Qiu, H. Zhou, H. Huang, H. Yang, M. Li, C. Gu, S. Xie, L. Qiao, L. Sun, *Adv. Mater.* **2010**, *22*, 999.
[17] K. Zhao, S. Li, G. Zan, G. Kim, W. Jiang, J. W. Park, J. Yoon, J. H. Oh, J. Jang, S. Lee, E. A. Shin, H. Kim, C. Park, *Nano Energy* **2024**, *126*, 109645.
[18] H. Xiang, L. Gao, D. Shi, L. Jiao, B. Cheng, N. Deng, G. Li, W. Kang, *Adv. Fiber Mater.* **2024**, *6*, 883.
[19] R. Xiong, H. S. Kim, S. Zhang, S. Kim, V. F. Korolovych, R. Ma, Y. G. Yingling, C. Lu, V. V. Tsukruk, *ACS Nano* **2017**, *11*, 12008.
[20] P. Zhu, Z. Yu, H. Sun, D. Zheng, Y. Zheng, Y. Qian, Y. Wei, J. Lee, S. Srebnik, W. Chen, G. Chen, F. Jiang, *Adv. Mater.* **2024**, *36*, 2306653.
[21] D. Ji, Y. Lin, X. Guo, B. Ramasubramanian, R. Wang, N. Radacsi, R. Jose, X. Qin, S. Ramakrishna, *Nat. Rev. Methods Prim.* **2024**, *4*, 1.
[22] S. Jayadevan, A. K. Aliyana, G. Stylios, *Nano Energy* **2024**, *129*, 110034.
[23] A. Levitt, S. Seyedin, J. Zhang, X. Wang, J. M. Razal, G. Dion, Y. Gogotsi, *Small* **2020**, *16*, 2002158.
[24] X. He, J. Gu, Y. Hao, M. Zheng, L. Wang, J. Yu, X. Qin, *Chem. Eng. J.* **2022**, *450*, 137937.
[25] Y, Liu, J. Song, Z. Liu, J. Chen, D. Wang, H. Zhi, J. Tang, Y. Zhang, N. Li, W. Zhou, M. An, H. Liu, G. Xue, *Nano-Micro Lett.* **2025**, *17*, 81.
[26] Y. Zhang, P. Wang, Q. Shi, X. Ning, Z. Chen, S. Ramakrishna, J. Zheng, Y. Long, *Adv. Fiber Mater.* **2025**, *7*, 374.
[27] A. Wang, C. Breakwell, F. Foglia, R. Tan, L. Lovell, X. Wei, T. Wong, N. Meng, H. Li, A. Seel, M. Sarter, K. Smith, A. Alvarez-Fernandez, M. Furedi, S. Guldin, M. M. Britton, N. B. McKeown, K. E. Jelfs, Q. Song, *Nature* **2024**, *635*, 353.
[28] W. Yuan, H. Liu, Y. Fu, Y. Zhang, H. Huo, L. Zhang, M. Yang, Y. Li, C. Chen, Y. Song, Z. Ling, *Chem. Eng. J.* **2024**, *499*, 155952.
[29] B. Shao, Y. Song, Z. Song, Y. Wang, Y. Wang, R. Liu, B. Sun, *Adv. Energy Mater.* **2023**, *13*, 2204091.
[30] Z. Zhang, Y. Zheng, N. Jiang, W. Hong, T. Liu, H. Jiang, Y. Hu, C. Li, *Sustain. Energy Fuels* **2022**, *6*, 2249.
[31] J. Zhang, P. Cui, J. Wang, Y. Ge, H. Meng, C. Feng, H. Liu, G. Cheng, Z. Du, *Adv. Mater. Tech.* **2023**, *8*, 2300370.
[32] M. Sajjad, M. A. Abdelsalam, A, Raza, F AlMarzooqi, T. Zhang, *Int. J. Heat Mass Transf.* **2024**, *223*, 125172.
[33] M. Wu, M. Peng, Z. Liang, Y. Liu, B. Zhao, D. Li, Y. Wang, J. Zhang, Y. Sun, L. Jiang, *ACS Appl. Mater. Inter.* **2021**, *13*, 26989.
[34] H. Guo, P. Yan, X. Sun, J. Song, F. Zhu, X. Guan, S. W. Sharshir, J. Shi, Z. Li, X. Xu, M. An, *Chem. Eng. J.* **2024**, *485*, 149918.
[35] G. Kresse, J. Furtmüller, *Phys. Rev. B* **1996**, *54*, 11169.
[36] P. E. Blöchl, *Phys. Rev. B* **1994**, *50*, 17953.
[37] J. P. Perdew, K. Burke, M. Ernzerhof, *Phys. Rev. Lett.* **1996**, *77*, 3865.
[38] B. Hammer, L. B. Hansen, J. K. Nørskov, *Phys. Rev. B* **1999**, *59*, 7413.